Design and Evaluation of Systemic Administration of Nano Silica MCM48:Eu³⁺ in Mouse Brain

Leandro A. Azevedo,[a,b] *Belmira L. S. Andrade-da-Costa,*[*,c] *Ricielle L. Augusto,*[c] *Leonis L. Luz,*[b] *Ivone A. de Souza,*[d] *Licarion Pinto,*[e] *Iane B. V. Alves*[*,b] *and Severino Alves Júnior*[*,a,b]

[a]*Pós-Graduação em Ciência de Materiais, Universidade Federal de Pernambuco (UFPE), 50670-901 Recife-PE, Brazil*

[b]*Departamento de Química Fundamental, Universidade Federal de Pernambuco (UFPE), 50670-901 Recife-PE, Brazil*

[c]*Departamento de Fisiologia e Farmacologia, Centro de Biociências, Universidade Federal de Pernambuco (UFPE), 50670-420 Recife-PE, Brazil*

[d]*Departamento de Antibióticos, Centro de Biociências, Universidade Federal de Pernambuco (UFPE), 50670-901 Recife-PE, Brazil*

[e]*Departamento de Química Analítica, Instituto de Química, Universidade do Estado do Rio de Janeiro (UERJ), 20550-013 Rio de Janeiro-RJ, Brazil*

In the present study, we tested the proof of concept that mobil mesoporous silica nanoparticle composition of matter (MCM) No. 48 doped with trivalent europium (nanoMCM48:Eu³⁺) administered systemically intravenously can act as a suitable vehicle to deliver neural cells to the brain of healthy adult Swiss mice without causing tissue damage. Moreover, we also tested the ability of this nanoparticle to release molecules *in vitro*, using as drug models caffeine or nicotine in phosphate buffer solution with pH 7.4 adequate to intra and extra-celular medium of the brain. The caffeine and nicotine adsorbed nanoparticles (CAF@MCM48:Eu³⁺ and NIC@MCM48:Eu³⁺) were observed in the parenchyma of the cerebral cortex and diffusely dispersed in the cellular cytoplasm. Statistical analysis using multivariate partner recognition methods indicated that there was no sign of cell damage, as it was characterized by chromatin condensation, nuclear condensation, or fragmentation. The characterization of nanoMCM48:Eu³⁺ as particle size, luminescent properties and release of active components were analyzed. The CAF@MCM48:Eu³⁺ and NIC@MCM48:Eu³⁺ nanoparticles were observed in the cerebral cortex parenchyma and diffusely dispersed in the cell cytoplasm, and the release of active components was analyzed. Therefore, the studies showed that mesoporous silica nanoparticles administered systemically via intravenous tissue can act as a suitable vehicle for neural cells in the brain of healthy mice without causing damage.

Keywords: proof of concept study, mesoporous silica nanoparticle, *in vivo* study, mouse brain, neural cells, systemic administration

Introduction

Drug delivery is an important pharmaceutic strategy for the treatment of various diseases because it optimizes pharmacokinetics and the pharmacodynamic effects of bioactive substances.[1,2] A suitable drug delivery system needs to have biocompatibility, ability to protect drugs from environmental degradation, region-specific action, high drug payload, and simultaneously controlled release function. All these properties improve pharmacological treatment.[3] A growing number of pre-clinical studies[4,5] have reported the use of nanomaterials to treat neurodegenerative diseases.

A favorable alternative to supply these drugs to the brain parenchyma involves a carrier-mediated controlled release which is capable of protecting the drug metabolization

and enable the crossing of the brain blood barrier (BBB) satisfactorily. It is worth mentioning that the BBB has selective permeability properties involving the size and liposolubility of the molecules which limit the delivery of a number of therapeutic agents proposed for neurological diseases.[6] To face this challenge, transport approaches based on silica nanoparticles for drug delivery have been indicated as an advanced therapeutic alternative for brain regions.[7]

The mesoporous silica nanoparticle of type Mobil composition of matter (MCM) No. 48 (MCM-48) is a potential candidate for drug transport because it presents adequate characteristics such as high surface area ratio/pore volume, a functionalized/modified surface, adjustable design and size, as well as properties such as biocompatibility and bioavailability in physiological concentrations.[7-9] Regarding the silica particles size, recent *in vitro* evidence has indicated that between 50-150 nm, the particles were non-toxic to human corneal epithelial cells or to retinal neural cells.[9] Mesoporous silica nanoparticles with nickel moieties and pore sizes between 25 and 30 nm were also developed to function as a safe proteasome transporter in HeLa cell lineage.[10] However, silica nanoparticles (SiNPs) between 5 and 15 nm were able to induce apoptosis in glioblastoma cells.[11] Despite these *in vitro* studies, there are recent *in vivo* studies reporting adverse effects of SiNPs with around 150 nm when they are intranasally administered.[12]

Using intravenous injection, other studies investigating the transport of mesoporous SiNPs throughout the BBB have reported controversy regarding its ability to achieve the brain parenchyma even after 48 h.[13] Using administration via carotid artery and analyzing the presence of polyethylene glycol (PEG) conjugated SiNPs after 1 or 3 h, Liu *et al.*[14] reported that the efficiency of BBB transport depends on the nanoparticle size. After systemic administration via intraperitoneal route of silica nanoparticles conjugated to [Ru(bpy)₃]Cl₂ dye and coated with glucose or glucose plus PEG, these particles were visualized in the brain tissue, but no evaluation of cytotoxicity was done.[15]

Therefore, the physico-chemical properties of SiNPs have been widely studied for application in the biomedical area, for the controlled release of a variety of pharmacologically bioactive molecules.[1] However, it is not still clear if systemic administration of SiNPs via intravenous route can cause cell damage into the brain parenchyma.

SiNPs type MCM48 doped with trivalent europium ion (nanoMCM48:Eu³⁺) also has luminescent properties that can be exploited in intracellular temperatures evaluation (as nanothermometers), imaging and drug release.[16] These luminescent properties make it possible to localize the presence of SiNPs within the cells.

Mesoporous silica contains free silanol groups on the surface and inside the pores, which facilitates absorption and biomolecular bonds, being attractive for adsorption and release of actives.[17,18] Caffeine (CAF) and nicotine (NIC) have organic groups, carbonyl, amides and amines, which form strong hydrogen bonds with silica, suggesting the use of biomolecules containing similar groups for drug delivery with this type of carrier.[19,20]

The main purpose of the present study was to test the hypothesis that mesoporous silica nanoMCM48:Eu³⁺ administered systemically can act as a nontoxic vehicle suitable for transport into the brain of healthy mice. Moreover, we also tested the ability of this nanoparticle to release bioactive molecules such as CAF or NIC in phosphate buffer solution with pH 7.4 adequate to intra and extracellular medium of the brain. We choose these bioactive substances considering recent *in vitro* and *in vivo* studies that have demonstrated the use of CAF and NIC as a promising alternative for the treatment of neurodegenerative diseases.[21,22] Nevertheless, to induce a therapeutic effect on cognition, the CAF plasma concentration needs to reach ca. 30 μM,[23,24] high doses, however, may cause adverse effects.[25] Systemic application of NIC as a therapeutic agent can also be limited by poor pharmacokinetic properties such as a short half-life in plasma, and potential adverse reactions.[26] Adequate doses of NIC for humans depends on the age, and in elderly patients with mild cognitive impairment, a NIC patch with 15 mg day⁻¹, for example, caused some mild gastrointestinal and neurological symptoms.[27] Thus, the investigation of potential nanoparticles for the delivery of NIC and CAF in the brain parenchima can be a promising alternative to attenuate side effects previously reported in the literature.

Experimental

Synthesis of the nanoparticles and adsorption and controlled release of the active components

The methodology of the synthesis of the nanoMCM48:Eu³⁺ and adsorption of CAF, NIC and controlled release *in vitro* (CAF@MCM48:Eu³⁺, NIC@MCM48:Eu³⁺) are present in the Supplementary Information (SI) section.

Characterization

The samples were characterized by X-ray diffraction (XRD, XRD-6000, Shimadzu, Kyoto, Japan) Cu Kα = 1.54056 Å, radiation at 40 kV and with a 30 mA filament with Ni filter, with step 0.01°, acquisition time of

1 s and angular window (2θ) of 1.5-8°. Scanning electron microscopy (SEM, SS-550 Superscan, Shimadzu, Kyoto, Japan) the macerated sample was placed on a carbon tape adhered to a metal support ("stub"), and these samples were covered with a thin layer of gold to make them conductive and improve the acquisition of microscopy images, operating in low vacuum, voltage of 30 kV, magnificence of 60.000 times. Transmission electron microscopy (TEM) was performed in a TECNAI 200 kV (FEI Company, Oregon, USA). For sample preparation, the nanoparticles were dispersed in ethanol (Dinâmica Ltda, Recife, PE, Brazil) and dripped onto copper grid with carbon film. Thermogravimetric analysis (TGA, DTG-60H, Shimadzu, Kyoto, Japan), solid samples were placed inside the balance under nitrogen atmosphere (White Martins, Cabo, PE, Brazil) with a heating rate of 10 °C min^{-1} with heating temperature up to 800 °C. For Fourier transform infrared spectroscopy (FTIR) Spectrum model 400 FT-IR/FT-NIR (PerkinElmer, Massachusetts, USA), a small sample were macerated with potassium bromide (KBr) and placed in a hydraulic press for 10 min to form a pellet. This tablet was attached to a support inside the FTIR through which it crosses a beam. The photoluminescent properties (excitation and emission spectra) of the compounds were studied at room temperature in powder form, the measurements were carried out in a spectrofluorimeter Model Fluorolog-3 ISA (Horiba Jobin Yvon, Kyoto, Japan). The apparatus is equipped with a monochromator double excitation and emission, model FL-1039/40. Continuous xenon lamps with a power of 450 W and pulsed xenon lamps of 150 W, photomultiplier R928P. Data were collected at a 90° angle in relation to the emission beam.

Animals and systemic treatment

A total of 48 adult male Swiss mice, obtained from different litters (2-3 pups *per* litter) were used. The animals were handled in accordance with the Ethics Committee for Animal Research of the Universidade Federal de Pernambuco, Brazil, (No. 23076.005404/2015-04) which complies with the "Principles of Laboratory Animal Care" (National Institutes of Health, Bethesda, USA).[28] The mice were kept in polypropylene cages (30.5 cm × 19.8 cm × 13.4 cm) in an animal house maintained at 22 ± 1 ℃ with a 12:12 h light-dark cycle (lights on at 6:00 a.m.) and fed a 23% protein lab chow diet (Purina Ltd, São Paulo, Brazil). Animals were divided in 4 groups (6 animals *per* group): control group received intravenous injection of 0.1 M phosphate buffer saline (PBS, pH 7.4) and the nanoMCM48:Eu^{3+}, CAF@MCM48:Eu^{3+} and NIC@MCM48:Eu^{3+} groups that received respectively intravenous injection 9.6 mg kg^{-1} of nanoMCM48:Eu^{3+}, 9.2 mg kg^{-1} caffeine associated with MCM48, 1 mg kg^{-1} nicotine associated with nanoMCM48:Eu^{3+}, all suspended in PBS. According to the body weight, the volume injected via tail vein ranged from 0.3 to 0.5 mL.

Animal perfusion and brain sectioning

Mice (six animals *per* group) were anesthetized with sodium pentobarbital (100 mg kg^{-1}, intraperitoneal (i.p.)) and perfused transcardially, first with saline (0.9% NaCl; 50 mL) followed by 4% paraformaldehyde (Sigma-Aldrich, São Paulo, Brazil) in a 0.1 M phosphate buffer (PB), pH 7.4 (200 mL). Perfusion was always carried out between 12 noon 6 pm, with a continuous infusion pump (Harvard equipment, Massachusetts, USA) at a rate of 7.64 mL min^{-1}. Thereafter, the brains were dissected starting from the prefrontal cortex back to the inferior limit of the brainstem. They were then post fixed for 2 h in the same fixative, rinsed in PB and subsequently, were cryoprotected in solutions containing increasing concentrations of sucrose in PB (10, 20 and 30%). Brain blocks were serially cut on a cryostat (Leica, São Paulo, Brazil) into 50 μm-thick sections across the parasagittal plane. All sections were collected serially in PB and arranged in six series. The stereotaxic atlas[29] was used to delimit the cytoarchitectonic regions. Some series of the free-floating sections were incubated for 5 min with Hoechst 33342 solution (1:1000) for labelling cell nuclei. After rinsed in PB, the sections were dried at 50 °C for 10 min, cleared in xylene (Sigma-Aldrich, São Paulo, Brazil) for 1 min and coverslipped with Entellan (Merck, Darmstadt, Germany).

Analysis of cell damage

Hoechst 33342 has been used to visualize cell damage and cell death indicated by chromatin condensation characterized by an increase in deoxyribonucleic acid (DNA) staining at the periphery of the nuclei, nuclear condensation (at least 50% smaller than control nuclei) nuclear fragmentation (both nuclear condensation and chromatin margination) both in the *in vivo* or *in vitro* assays.[30] Therefore, morphometric analyses of cell nuclei size and fluorescence intensity to indicate chromatin condensation were carried out in serial brain sections of 3-4 animals *per* group (control, nanoMCM48:Eu^{3+}, CAF@MCM48:Eu^{3+} and NIC@MCM48:Eu^{3+}) in layers 3 and 4 of the parietal cerebral cortex. Digital images of the brain sections were obtained using a trinocular epifluorescence microscope (DM 5500-B, Leica, São Paulo, Brazil). Using G ∗Power software (version 3.19.7),[31]

a statistical power analysis was made to estimate the sampling area required to generate the results. Three randomly selected microscope fields *per* brain section and three sections were analyzed for each animal (9 fields × 3 animals = 27) to detect a large effect size (effect size (f) = 0.481) with 80% confidence (power = 0.8). Each field represented a sampling area of 0.310 × 0.230 mm (0.0713 mm²) which means 0.2139 mm² of total area analyzed in the layers 3 and 4 of the parietal cerebral cortex.

Images of 630× magnification were used to quantify the fluorescence intensity. Using the chemometrics analysis of Hoechst 33342, potential cell damage was evaluated, characterized by chromatin condensation, nuclear condensation or fragmentation.

A principal component analysis (PCA)[32] was used to identify the pattern of the chemical image fluorescence to see if there had been any damage to the analyzed cells.

Two types of statistical analysis were performed with this data. In one, the cell area and the perimeter were obtained using ImageJ software, version 1.48 (NIH)[33] and a statistical analysis of a normal distribution histogram was carried out using program R.[34,35] Thereafter, a pattern recognition was performed to evaluate if there were any

abnormalities in the area and to establish the perimeter profile between the groups. In the second analysis, PCA was made directly from the color histogram[36,37] of the randomly selected cells (90 cells/field and 270 cells *per* animal) in the images. The color histograms were obtained using a customized processing programs developed for the Matlab[38] environment. All the graphics presented in chemometrics analysis were prepared in a MatLab 2010b environment. The PCA analysis was performed in MatLab 2010b[38] using PCA toolbox.[39] PCA has been recently used as a novel approach to generate a highly sensitive compound score for cell analysis in brain sections.[40] In the present study, this statistical analysis was adopted especially due to its ability to evaluate pattern recognition and subtle differences in nuclei size and fluorescence intensity between the groups.[32]

Results and Discussion

Physico-chemical characterization of nanoMCM48:Eu³⁺

The morphology of the nanoMCM48:Eu³⁺ was visualized using SEM (Figure 1a) and TEM (insert in Figure 1a).
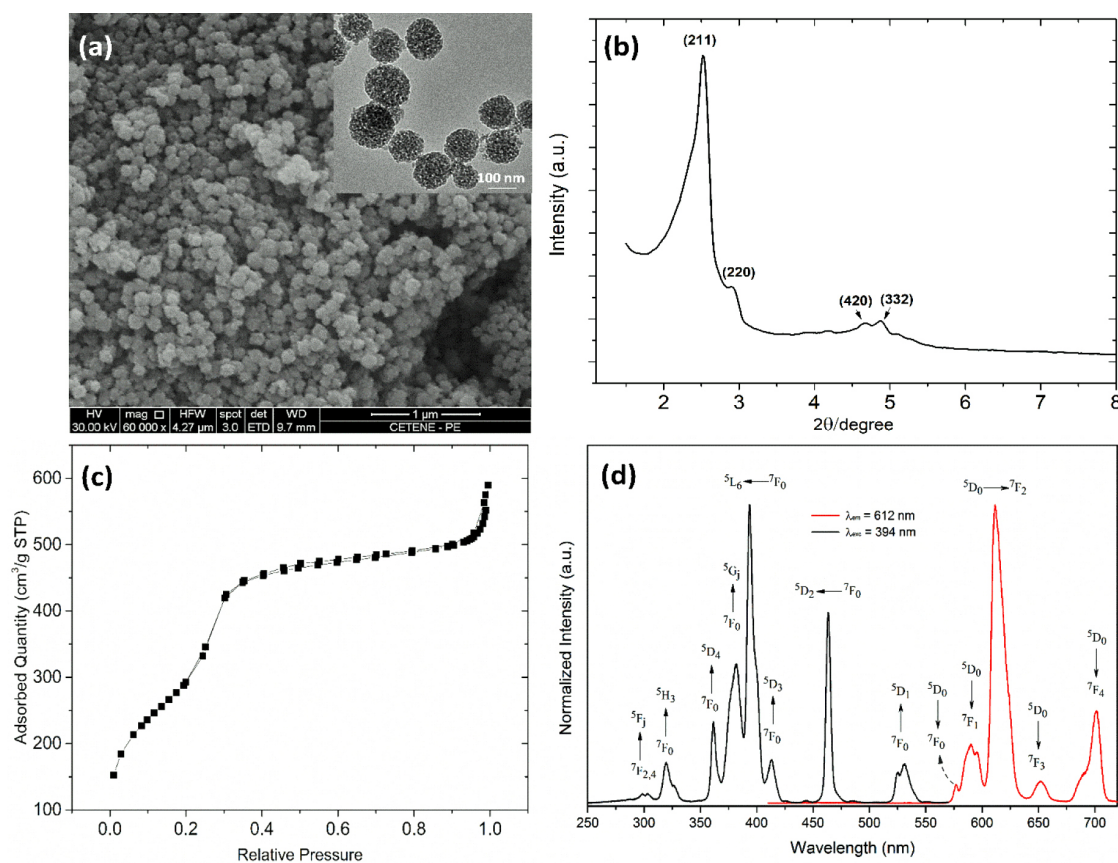
Figure 1. (a) Scanning electron microscopy (SEM) and transmission electron microscopy (TEM) (insert) of nanoMCM48:Eu; (b) X-ray diffraction (XRD) with a pitch of 0.01° s⁻¹ in the range of 1.5-8° nanoMCM48:Eu³⁺; (c) nano sorption isotherm of nanoMCM48:Eu³⁺ and (d) excitation spectra (black lines; λ_{em} = 612 nm) and emission (red line; λ_{ex} = 394 nm) of nanoMCM48:Eu³⁺.

A spherical pattern with a homogeneous distribution and sizes around 121 nm (Figure S1, SI section) are typical features of this material, in accordance with the literature.[41] The size range was also within the limits considered non-toxic for neural tissue[42] and suitable for systemic administration. The XRD in Figure 1b showed diffraction peaks at (211), (220), (420) and (332) characteristic of MCM48-type silica.[14]

The shape of the isotherm for nanoMCM48:Eu³⁺ in Figure 1c a was shown to be type IV, characteristic for mesoporous materials that have pore size between 2-50 nm according to literature.[43] In this material, the appearance of a hysteresis between the branches of adsorption and desorption in the isotherm is characteristic, as shown in Figure 1c.[44] A narrow hysteresis profile was observed, indicating that pore sizes were around 4 nm, as expected for this type of silica.[43,44]

The photoluminescent properties of nanoMCM48:Eu³⁺ (Figure 1d) were investigated in solid state and at room temperature. The excitation spectrum (black line), obtained by monitoring emission monitoring at 612 nm ($^5D_0 \rightarrow {}^7F_2$), presents bands centered at 525, 464, 415, 394, 382, 376, 362, 320 and 300 nm, associated with transitions $^7F_0 \rightarrow {}^5D_1$, $^5D_2$, $^5D_3$, $^5L_6$, $^5G_2$, $^5G_4$, $^5D_4$, ^5H_J and ^5F_J, from the Eu³⁺ ion, respectively. The emission spectrum (red line) presents a spectral profile related to the transitions $^5D_0 \rightarrow {}^7F_J$, at J = 0, 1, 2, 3 and 4, typical of compounds containing Eu³⁺ ions in low symmetry environment.[45] The transition $^5D_0 \rightarrow {}^7F_0$ occurs by mixing the state $^7F_0$ with the states $^7F_2$, $^7F_4$ and $^7F_6$, and suggests that that the Eu³⁺ ion is in an environment with symmetry C_1, Cn or Cnv.[45]

Quantification of caffeine and nicotine adsorption on nanoMCM48:Eu³⁺

The linear function obtained from the calibration curves (Figure S2, SI section) served as a parameter to quantify the adsorption rates of the CAF and NIC drugs (Figure 2a), 69.5 and 85.1%, respectively, as registered on Table S1 (SI section), which significantly outperformed the formulations of other silicate systems as found in other works.[19,46-48] In addition, this high adsorption rate of the drugs used here is an important data to determine the efficiency of the CAF@MCM48:Eu³⁺ and NIC@MCM48:Eu³⁺ systems as sustained release vehicles.[49-51] The thermograms in Figure 2b confirmed the presence and amount of CAF and NIC in the respective mesoporous structures. NIC had a more efficient loading than caffeine, due to the molecular characteristics of its structure, such as a greater degree of freedom, hydrogen bonds and less hysterical impediment.
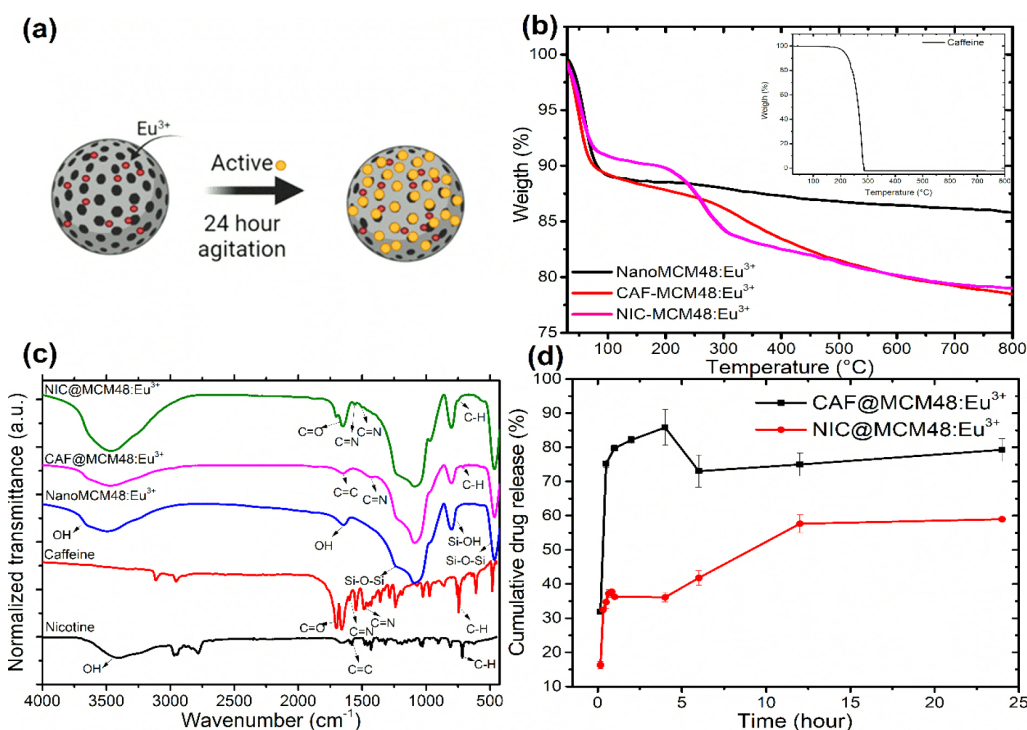
Figure 2. (a) Caffeine and nicotine adsorption scheme; (b) thermogravimetric events in nitrogen gas atmosphere (N₂) at 10 °C *per* min, a temperature rise in the ambient temperature range up to 800 °C of the following components: caffeine, nanoMCM48:Eu³⁺, CAF@MCM48:Eu³⁺, NIC@MCM48:Eu³⁺; (c) FTIR spectra in KBr pellets of the systems: nicotine, caffeine, nanoMCM48Eu³⁺, NIC@MCM48:Eu³⁺, CAF@MCM48:Eu³⁺ and (d) release kinetics caffeine, nicotine. System monitored 24 h under 100 rpm agitation in PBS medium.

Physico-chemical characterization of CAF@MCM48:Eu³⁺ and NIC@MCM48:Eu³⁺

Figure 2b shows the thermogravimetric events of the caffeine (inserted Figure 2b) and the nanoMCM48:Eu³⁺ associated with CAF or NIC. In the nanoMCM48:Eu³⁺, there was a visible event in the region up to 110 °C, which represents mass loss, attributed to water. The caffeine alone was characterized by an event between 193-291 °C, with loss of mass around 98.6%. This characteristic of caffeine mass loss is due to sublimation in this temperature interval. In the CAF@MCM48:Eu⁺³, two mass losses were seen: 28% between 180 and 389 °C and 15% between 157 and 382 °C. Regarding the NIC@MCM48Eu³⁺, the mass loss was 21% between 127 and 290 °C, attributed to nicotine, corroborating with the standard described in the literature.[33]

In the nicotine FTIR spectrum (Figure 2c), frequencies of carbon sp² (vC=C) in 1600 cm⁻¹ and in the bands from 700 to 800 cm⁻¹ are observed. The aliphatic part of the molecule is present as very strong vibrations due to the hydrogen-carbon (C−H) bonds present in the bands 3000-2800 cm⁻¹.[52] At 3400 cm⁻¹, the band hydroxyl (−OH) responsible for the water molecules in the nicotine solution is recorded.

In the caffeine FTIR spectrum (Figure 2c), the peak in the region of 2977 cm⁻¹ is attributed to bonding vibration (vC−H) and in 2924 cm⁻¹ it is attributed to the asymmetric vibrations of methyl sp³ carbon (v_{as}CH₃).[52] The bands in the regions of 1655 and 1599 cm⁻¹ are related to (C−C) and (C=N) linkages, respectively. In the 1700 cm⁻¹ region, it is associated to carbonyl (C=O). Peaks between 1449 and 1346 cm⁻¹ are due to the stretching of methyl (δCH₃).[52] The bands observed between 1100-1000 cm⁻¹ region are related to the vibration in the deformation plane of the heterocyclic compounds. The mean strong vibration is attributed to the bands at 862 and 800 cm⁻¹, which are consequences of the N=C−H and N−C−H bonds due to the vibrations occurring in the imidazole ring.[53]

The FTIR spectrum of nanoMCM48:Eu³⁺ (Figure 2c) shows the band at 464 cm⁻¹ corresponding to the stretching of the silicon and oxygen bond (δSi−O−Si). In 965 cm⁻¹, a silanol group vibration band (vSi−OH) is observed, and at 1094 cm⁻¹, the band is assigned to asymmetric vibration (v_{as} Si−O−Si). In the regions of 3500 and 1653 cm⁻¹ the vibrations are originated from the absorption of water molecules indicating the presence of hydroxyl groups (−OH) on the surface.[54]

In the NIC@MCM48:Eu³⁺ FTIR spectrum (Figure 2c), the presence of nicotine is visualized in two regions. In the region 1600 cm⁻¹ with the vibration of the carbon sp² (vC=C) and in the region of 790 cm⁻¹ due to the carbon-hydrogen (vC−H) bonds. For the system CAF@MCM48:Eu³⁺, we observed 3 bands attributed to caffeine: carbonyl (C=O) in the region of 1700 cm⁻¹, and the vibrations due to methyl (CH₃) in the region (1580 cm⁻¹) and in the region of 800 cm⁻¹ as a result of the flexion of the C−H bond.

The release kinetics curve for the caffeine and nicotine activities showed two notable segments, representing two different release rates (Figure 2d). For caffeine, there was an intense and rapid release, the so-called burst effect, which occurs in the bloodstream in the first minutes of contact with the external environment.[55]

Then, this substance showed a 79% more sustained release over the next 20-25 h. Regarding the system with nicotine, there was a more conventional behavior in the context of MCM-48.[56] In this assay, a release rate of 60% was found. Thus, the release profiles obtained reflected a significant control of the systems under study, showing that they played a fundamental role in the release rate of the pharmacological substances in question.

Visualization of nanoparticles in the cerebral cortex

Figure 3a shows the emission spectrum of the nanoMCM48:Eu³⁺ which was obtained upon excitation of the europium ion at 394 nm, at room temperature and in the solid state. This spectrum revealed the presence of nanoMCM48:Eu³⁺ in the cerebral cortex, mainly visualized with filters with emission spectra in red (598 nm, Figure 3b) and some particles also detected using green filters with emission at 488 nm (Figure 3c).

The emission spectra of NIC@MCM48:Eu³⁺ or CAF@MCM48:Eu³⁺ were obtained with excitation at 393 and 394 nm, respectively, at room temperature, in the solid state (Figures 4a and 4d).

The presence of NIC@MCM48:Eu³⁺ or CAF@MCM48:Eu³⁺ nanoparticles in the cerebral cortex parenchyma was detected according to emission spectral region of red (Figure 4b and 4e) and green (Figures 4c and 4f).

Z-stack images were obtained from brain sections of NIC@MCM48:Eu³⁺ (Figures 5d-5f) and CAF@MCM48:Eu³⁺ (Figures 5a-5c) animal groups. The double labeling for Hoechst indicated the presence of both nanoparticles around the cell nuclei.

Morphometric and chemometric analysis of potential cell damage induced by the nanoparticles in the brain parenchyma

In the cerebral cortex of the mice treated with nanoMCM48:Eu³⁺ associated or not with either CAF or NIC, no signs of cell nuclei damage, or marginal
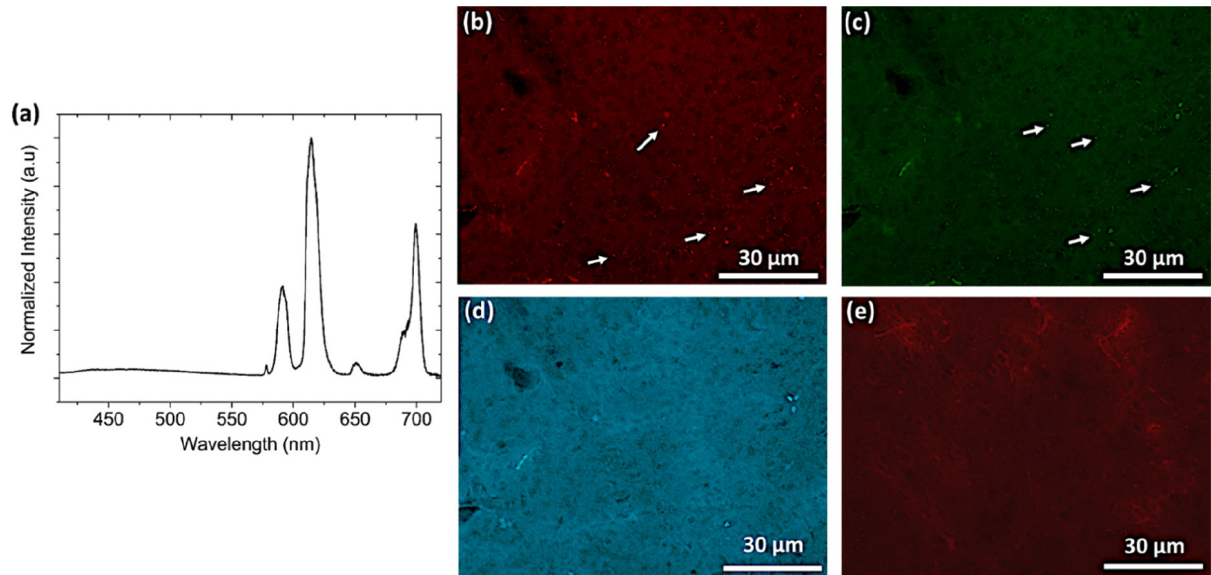
Figure 3. (a) Emission spectra of the nanoMCM48:Eu³⁺ with excitation at 394 nm. Visualization of nanoparticles in the cerebral cortex: (b) filters with emission spectra in red at 598 nm; (c) green filters with emission at 488 nm; (d) emission in the blue wavelength 410 nm and (e) filters with emission spectra in the red at 598 nm in brain of the animal group injected only with PBS.
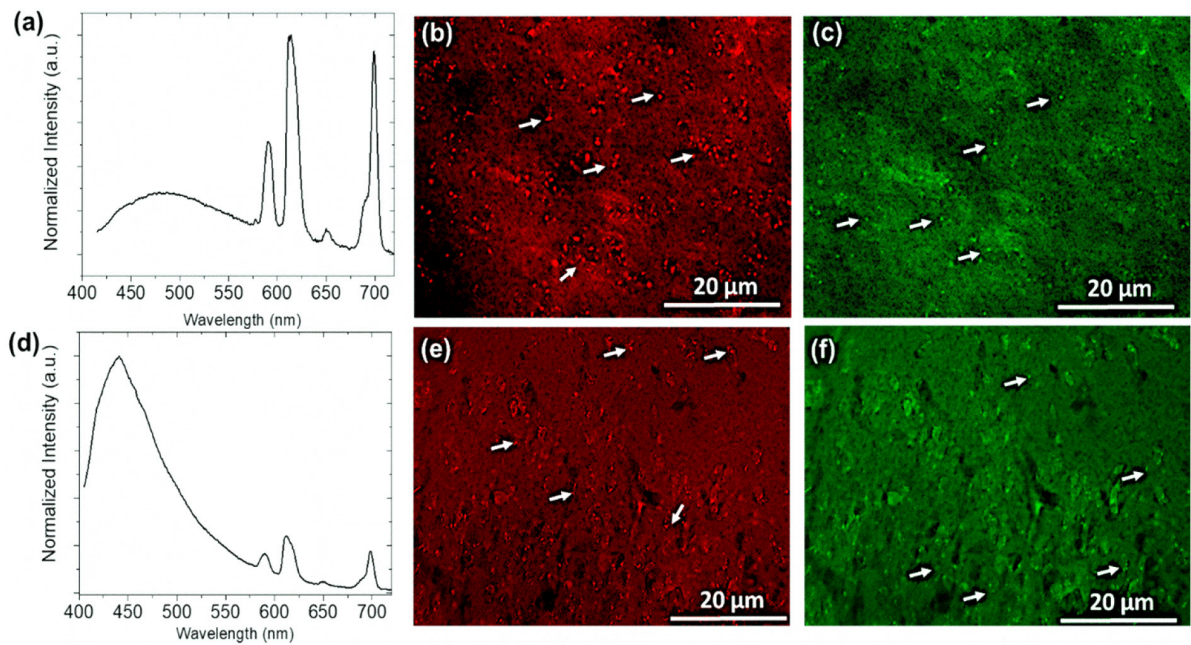
Figure 4. (a and d) Emission spectra of the NIC@MCM48:Eu³⁺ or CAF@MCM48:Eu³⁺ with excitation at 393 and 394 nm. NIC@MCM48:Eu³⁺ and CAF@MCM48:Eu³⁺ nanoparticles into the cerebral cortex (Figures 4b and 4e) and green (Figures 4c and 4f).

chromatin were detected compared to the control condition (Figures 6a-6d).

Morphometric analysis

The nuclei area and perimeters from a total of 2603 cells from nanoMCM48:Eu³⁺, CAF@MCM48:Eu³⁺ or NIC@MCM48:Eu³⁺ groups were measured using the ImageJ software.[33] Initially, a Shapiro-Wilk normality test was applied, and a normal distribution was confirmed for all cells. Histograms of the cell nuclei area and perimeter of all analyzed cells were built (Figure 7). The mean values for nuclei perimeter or area did not show intergroup differences at 95% of confidence.

This initial analysis showed that no nuclei size modification indicative of pyknosis was induced by the silica nanoparticles in the cortical heterogeneous neural cell populations. Moreover, a 2D plot of mean area and perimeter values indicated that there was a natural variation in the cell nuclei size, but the distribution detected
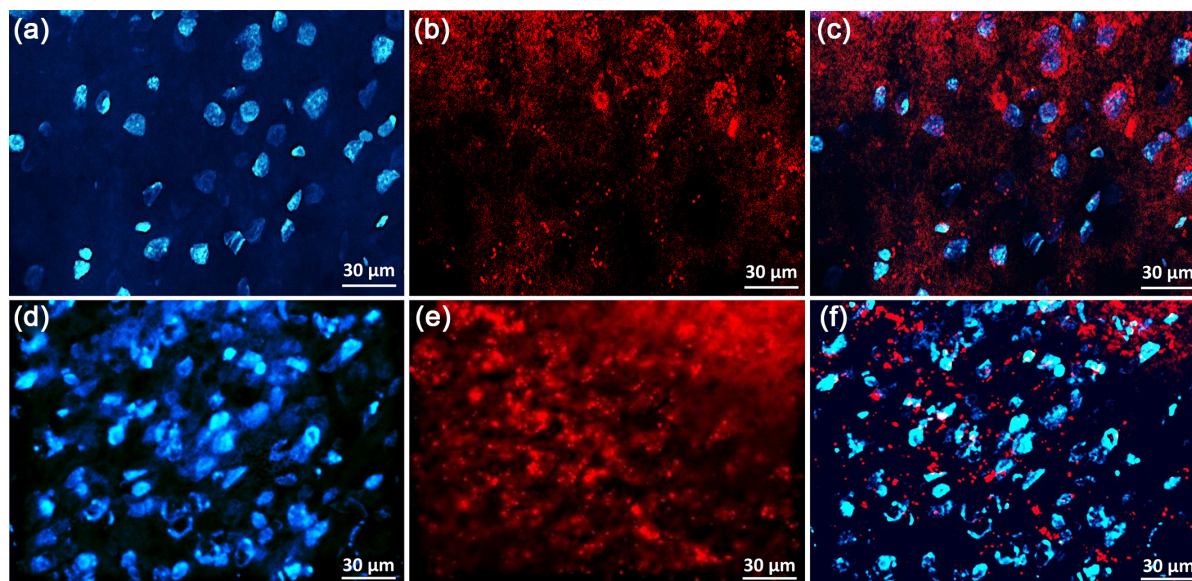
Figure 5. Z-stack images from parasagittal brain sections of a representative animal from the CAF@MCM48:Eu³⁺ group labeled for Hoechst 33342 (a) nanoparticles (b) and both (merge in c), and z-stack images from parasagittal brain sections of a representative animal from the NIC@MCM48:Eu³⁺ group labeled for Hoechst 33342 (d) and nanoparticles (e) and both (merge in f). Note the presence of the nanoparticles around the nuclei.
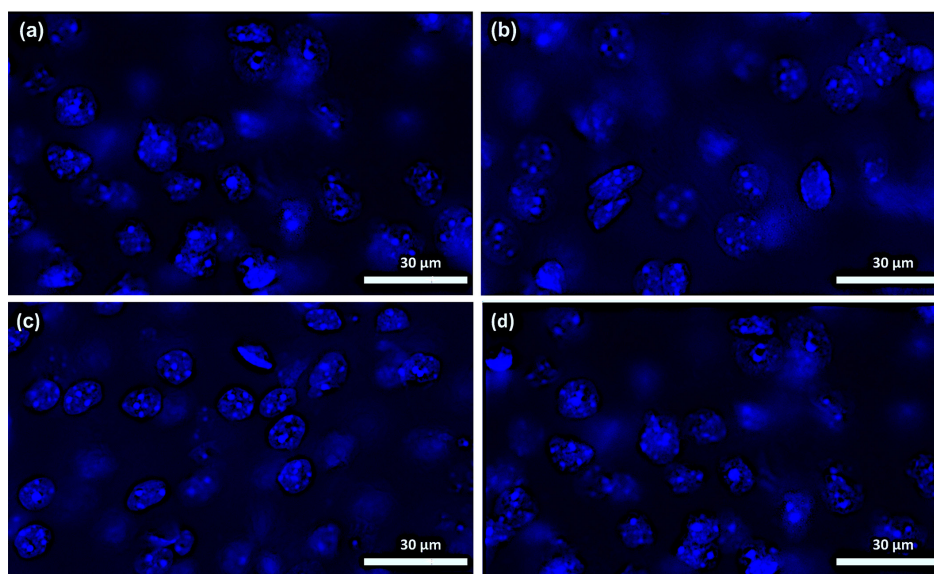
Figure 6. (a) Images from parasagittal brain sections of representative animals from the control, (b) nano MCM48:Eu³⁺, (c) CAF@MCM48:Eu³⁺ and (d) NIC@MCM48:Eu³⁺ groups labeled for Hoechst 33342. Note the absence of signs indicative of cell nuclei damage or marginal chromatin.

in the nanoMCM48:Eu³⁺, CAF@MCM48:Eu³⁺ and NIC@MCM48:Eu³⁺ groups were in the same range (Figure 7). The linear relationship observed in this 2D plot indicates the correlation between the area (πr^2) and perimeter ($2\pi r$) of a circle and shows that all analyzed cell nuclei display a circular shape, so reinforcing the observation that abnormalities on the nuclei shape were also not present.

Chemometric analysis

A total of 557 cell nuclei from 105 images of nanoMCM48:Eu³⁺, CAF@MCM48:Eu³⁺ and the NIC@MCM48:Eu³⁺ groups were analyzed using Hoechst 33342 to investigate cell damage as would be indicated by chromatin condensation or disorganization (Figure 8). The cell nuclei were analyzed using a customized processing program developed for Matlab where each cell is individually selected and converted in a histogram of gray, red, green, blue, hue, and saturation value scales as a result of the fluorescence of bisbenzimide (2-(4-ethoxyphenyl)-6-[6-(4-methylpiperazin-1-yl)-1*H*-benzimidazol-2-yl]-1*H*-benzimidazole).

Two PCAs were performed in this data: one using the mean histogram for each group and the other
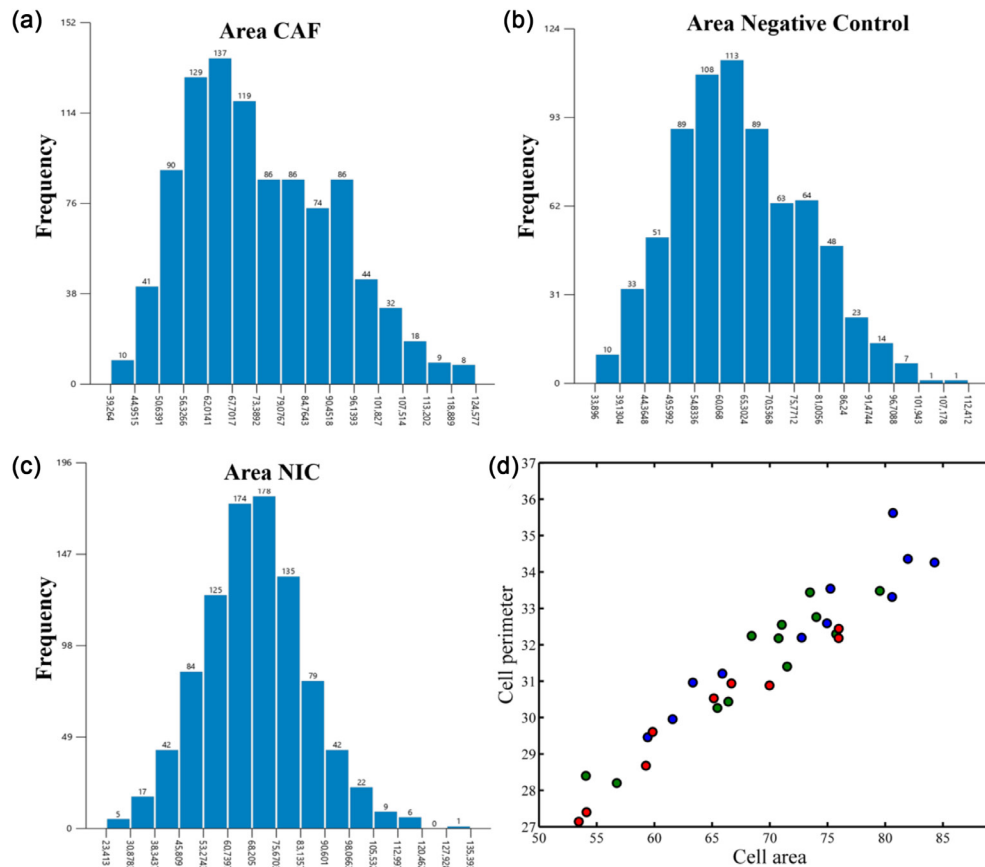
Figure 7. (a) Frequency histogram distribution for CAF, (b) negative control (NC) and (c) NIC groups. (d) Linear relation between mean cell area and perimeter values for each mice brain cut of CAF, NC and NIC groups, respectively colored as blue, red and green circles.

using each cell as an individual sample. According to the findings shown in Figure 7, no differences between nanoMCM48:Eu^{3+}, CAF@MCM48:Eu^{3+} or NIC@MCM48:Eu^{3+} groups were detected when compared to the control condition. However, when each individual cell was analyzed, it was observed that one cell, in sample 84, presented a higher hue value and one cell in the sample 442 shows lower values when compared to the other 555 cells. The image of these samples can be observed in the SI section, where sample 84 is highlighted by red circle and the sample 442 with green circle. No signal of either chromatin disorganization or condensation was detected in any of the samples.

The development of new mesoporous silica nanoparticles for biomedical use entails close attention to safety issues, considering their high surface area which may also affect the biocompatibility due to high reactivity.[57] In addition, the pore architecture of silica nanoparticles also affects the biocompatibility and needs to be carefully designed. Although the biocompatibility of SiNPS has been extensively studied in various biological systems, currently, there is limited data regarding the safety and biocompatibility of SiNPS in brain tissue, whether under

healthy or neurodegenerative and neuroinflammatory conditions.[58]

The absence of apoptotic cell death induced by nanoMCM48:Eu in cortical neural cells reinforces the safety properties of mesoporous silica for biomedical applications, in agreement with what has been reported in macrophages[59] or in rat pheochromocytoma PC12 cells.[57,60] In this latter study, even after a whole day of exposing PC12 cells to mesoporous silica nanoparticles, no significant DNA damage or reduction of cell viability was detected when compared to the control condition. The mesoporous configuration exhibits better biocompatibility than colloidal silica nanoparticles especially considering aspects such as apoptotic cell death and inflammatory responses.[59]

The present findings *in vivo* using the nanoMCM48:Eu^{3+} with a 100-140 nm diameter (Figure S1, SI section) indicate its safety properties and its ability to be clearly visualized in the brain parenchyma. These data are in agreement with the previous evidence demonstrating the ability of surface modified silica nanoparticles using the fluorescent [Ru(bpy)$_3$]Cl$_2$ dye marker to cross the brain-blood barrier.[15] Moreover, they also reinforce our initial hypothesis that nanoMCM48:Eu^{3+} can be a safety carrier and achieve the
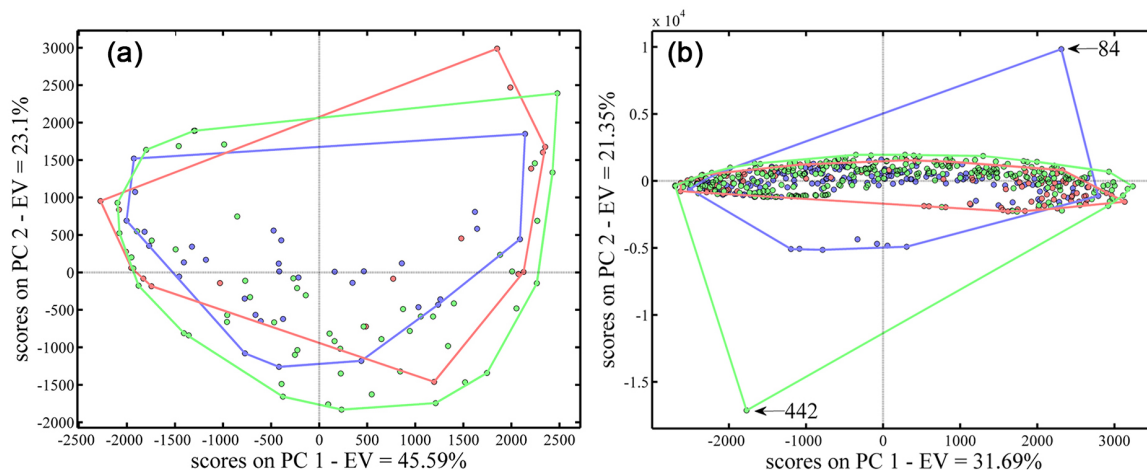
Figure 8. Principal component analysis using the means of the 105 images (a) and for all of the 557 individually analyzed cells (b). CAF, NC and NIC groups, respectively colored as blue, red and green circles and the groups with lines in the same colors. The lines were built by connecting the outermost samples.

cell cytoplasm without affecting the nucleus viability, which is also a positive aspect of their functionality.

Conclusions

The studies showed that mesoporous silica nanoparticle administered systemically via intravenous tissue can act as a suitable vehicle for neural cells in the brain of healthy mice without causing damage. The findings indicate that the europium ion (Eu³⁺) can be used as spectroscopic probe when associated to silica, opening up perspectives for its future use aiming to analyze real time drug delivery and cell interactions. It is noteworthy to reinforce that the adsorption of the nanoMCM48:Eu³⁺ with nicotine or caffeine did not modify the properties of this nanoparticles as a potential carrier.

Supplementary Information

Supplementary data (synthesis of nanoMCM48:Eu³⁺, adsorption of CAF@MCM48:Eu³⁺ and NIC@MCM48:Eu³⁺, release kinetics, photoluminescence spectrum: caffeine, CAF@MCM48:Eu³⁺, nicotine, NIC@MCM48:Eu³⁺ and histogram of nanoMCM48:Eu³⁺ particle distribution) are available free of charge at http://jbcs.sbq.org.br as PDF file.

Acknowledgments

Author Contributions

Leandro A. de Azevedo was responsible for making the materials, characterization, adsorption and release of caffeine and nicotine conceptualization, data curation, formal analysis, investigation and methodology, project management and write the original draft; Leonis L. Luz for the photoluminescence analyses, investigation and characterization of the materials; Belmira L. S. Andrade-da-Costa for animals, systemic treatment, animal perfusion and brain sectioning and cell damage analysis and writing, project administration, conceptualization and correction of the original draft; Ricielle L. Augusto for animal perfusion and brain sectioning and cell damage analysis; Licarion Pinto for analysis of cell damage by principal component analysis (PCA), research, methodology, data curation, formal analysis, and PCA data writing and figures; Iane B. V. Alves and Severino Alves Júnior for analysis, obtaining funding, research methodology, design administration and writing and revision of the original draft, conceptualization, formal analysis, funding acquisition, investigation, methodology, project management, write and revise the original draft.

References

1. Kwon, S.; Singh, R. K.; Perez, R. a; Abou Neel, E. a; Kim, H.-W.; Chrzanowski, W.; *J. Tissue Eng.* **2013**, *4*. [Crossref]

2. Nguyen, T.-T.-L.; Maeng, H.-J.; *Pharmaceutics* **2022**, *14*, 572. [Crossref]

3. Thassu, D.; Deleers, M.; Pathak, Y. V. In *Nanoparticulate Drug Delivery Systems*; Thassu, D.; Deleers, M.; Pathak, Y. V., eds.; CRC Press: Boca Raton, 2007, ch. 6. [Crossref]

4. Bhattacharya, T.; e Soares, G. A. B. E.; Chopra, H.; Rahman, M. M.; Hasan, Z.; Swain, S. S.; Cavalu, S.; *Materials* **2022**, *15*, 804. [Crossref]

5. Nguyen, K. T.; Pham, M. N.; Van Vo, T.; Duan, W.; Tran, P. H.-L.; Tran, T. T.-D.; *Curr. Drug Metab.* **2017**, *18*, 786. [Crossref]

6. Villabona-Rueda, A.; Erice, C.; Pardo, C. A.; Stins, M. F.; *Front. Cell. Neurosci.* **2019**, *13*, 405. [Crossref]

7. Song, Y.; Du, D.; Li, L.; Xu, J.; Dutta, P.; Lin, Y.; *ACS Appl. Mater. Interfaces* **2017**, *9*, 20410. [Crossref]

8. Wang, Y.; Zhao, Q.; Han, N.; Bai, L.; Li, J.; Liu, J.; Che, E.; Hu, L.; Zhang, Q.; Jiang, T.; Wang, S.; *Nanomedicine* **2015**, *11*, 313. [Crossref]

9. Park, J.-H.; Jeong, H.; Hong, J.; Chang, M.; Kim, M.; Chuck, R. S.; Lee, J. K.; Park, C.; *Sci. Rep.* **2016**, *6*, 37762. [Crossref]

10. Murugadoss, S.; Lison, D.; Godderis, L.; Brule, S.; Van Den Mast, J.; Brassinne, F.; Sebaihi, N.; Hoet, P. H.; *Arch. Toxicol.* **2017**, *91*, 2967. [Crossref]

11. Naumowicz, M.; Krętowski, R.; Naumowicz, M.; Stypułkowska, A.; Cechowska-Pasko, M.; *Int. J. Nanomed.* **2018**, *13*, 2279. [Crossref]

12. Yuan, X.; Yang, Y.; Xia, D.; Meng, L.; He, M.; Liu, C.; Zhang, Z.; *Front. Neurosci.* **2022**, *15*, 807988. [Crossref]

13. Baghirov, H.; Karaman, D.; Viitala, T.; Duchanoy, A.; Lou, Y. R.; Mamaeva, V.; Pryazhnikov, E.; Khiroug, L.; Davies, C. L.; Sahlgren, C.; Rosenholm, J. M.; *PLoS One* **2016**, *11*, e0160705. [Crossref]

14. Liu, C.; Wang, S.; Rong, Z.; Wang, X.; Gu, G.; Sun, W.; *J. Non-Cryst. Solids* **2010**, *356*, 1246. [Crossref]

15. Tamba, B. I.; Streinu, V.; Foltea, G.; Neagu, A. N.; Dodi, G.; Zlei, M.; Tijani, A.; Stefanescu, C.; *Arabian J. Chem.* **2018**, *11*, 981. [Crossref]

16. Syamchand, S. S.; Sony, G.; *J. Lumin.* **2015**, *165*, 190. [Crossref]

17. Knopp, D.; Tang, D.; Niessner, R.; *Anal. Chim. Acta* **2009**, *647*, 14. [Crossref]

18. Vallet-Regí, M.; Schüth, F.; Lozano, D.; Colilla, M.; Manzano, M.; *Chem. Soc. Rev.* **2022**, *51*, 5365. [Crossref]

19. Liédana, N.; Marín, E.; Téllez, C.; Coronas, J.; *Chem. Eng. J.* **2013**, *223*, 714. [Crossref]

20. Iwenofu, J. C.: *The Use of Silica Nanoparticles for Controlled Drug Delivery of Nicotine*; PhD thesis, Georgia Southern University: Georgia, 2022. [Link] accessed in April 2023

21. Rezvani, a H.; Levin, E. D.; *Biol. Psychiatry* **2001**, *49*, 258. [Crossref]

22. Aoyama, K.; Matsumura, N.; Watabe, M.; Wang, F.; Kikuchi-Utsumi, K.; Nakaki, T.; *Neuroscience* **2011**, *181*, 206. [Crossref]

23. Costenla, A. R.; Cunha, R. A.; de Mendonça, A.; *J. Alzheimer's Dis.* **2010**, *20*, S25. [Crossref]

24. Echeverria, V.; Zeitlin, R.; *CNS Neurosci. Ther.* **2012**, *18*, 517. [Crossref]

25. Kolahdouzan, M.; Hamadeh, M. J.; *CNS Neurosci. Ther.* **2017**, *23*, 272. [Crossref]

26. Sobieraj, D. M.; White, W. B.; Baker, W. L.; *J. Am. Soc. Hypertens.* **2013**, *7*, 61. [Crossref]

27. Newhouse, P.; Kellar, K.; Aisen, P.; White, H.; Wesnes, K.; Coderre, E.; Pfaff, A.; Wilkins, H.; Howard, D.; Levin, E. D.; *Neurology* **2012**, *2*, 91. [Crossref]

28. National Institutes of Health (NIH); *Guide for the Care and Use of Laboratory Animals*, 8th ed.; The National Academies Press: Washington, 2011. [Link] accessed in April 2023

29. Paxinos, G.; Watson, C.; Pennisi, M.; Topple, A.; *J. Neurosci. Methods* **1985**, *13*, 139. [Crossref]

30. Zhao, X.; Pike, B. R.; Newcomb, J. K.; Wang, K. K. W.; Posmantur, R. M.; Hayes, R. L.; *Neurochem. Res.* **1999**, *24*, 371. [Crossref]

31. *G.Power*, 3.19.7; Heinrich-Heine-University Software, Apps, and Games Free Download, Germany, 2020. [Link] accessed in April 2023

32. Bro, R.; Smilde, A. K.; *Anal. Methods* **2014**, *6*, 2812. [Crossref]

33. Rasband, W. S.; *ImageJ*, version 1.48 (NIH); U. S. National Institutes of Health, Bethesda, Maryland, USA, 1997-2018. [Link] accessed in April 2023

34. Darzé, B. C.; Lima, I. C.A.; Pinto, L.; Luna, A. S.; *Chemom. Intell. Lab. Syst.* **2022**, *231*, 104696. [Crossref]

35. Darzé, B. C.; Lima, I. C.A.; Pinto, L.; Luna, A. S.; *Chemom. Intell. Lab. Syst.* **2023**, *237*, 104810. [Crossref]

36. Diniz, P. H. G. D.; *J. Chemom.* **2020**, *34*, e3242. [Crossref]

37. Prats-Montalbán, J. M.; de Juan, A.; Ferrer, A.; *Chemom. Intell. Lab. Syst.* **2011**, *107*, 1. [Crossref]

38. *Matlab*, version 10b; The MathWorks Inc.; Natick, MA, USA, 2010. [Link] accessed in April 2023

39. Ballabio, D.; *Chemom. Intell. Lab. Syst.* **2015**, *149*, 1. [Crossref]

40. Heindl, S.; Gesierich, B.; Benakis, C.; Llovera, G.; Duering, M.; Liesz, A.; *Front. Cell. Neurosci.* **2018**, *12*, 106. [Crossref]

41. Kim, T.-W.; Chung, P.-W.; Lin, V. S.-Y.; *Chem. Mater.* **2010**, *22*, 5093. [Crossref]

42. Suh, W. H.; Suslick, K. S.; Stucky, G. D.; Suh, Y. H.; *Prog. Neurobiol.* **2009**, *87*, 133. [Crossref]

43. Robertson, C.; Lodge, A. W.; Basa, P.; Carravetta, M.; Hector, A. L.; Kashtiban, R. J.; Sloan, J.; Smith, D. C.; Spencer, J.; Walcarius, A.; *RSC Adv.* **2016**, *6*, 113432. [Crossref]

44. Rodrigues, V. M.: *Simulação Computacional de um Sistema de Refrigeração de Adsorção Acionado por Gases Quentes de Exaustão*; MSc. Dissertation, Universidade Estadual de Campinas, Campinas, 2013. [Link] accessed in April 2023

45. Binnemans, K.; *Coord. Chem. Rev.* **2015**, *295*, 1. [Crossref]

46. Dolinina, E. S.; Parfenyuk, E. V.; *J. Solid State Chem.* **2014**, *209*, 105. [Crossref]

47. Quintero-Jaramillo, J. A.; Carrero-Mantilla, J. I.; Sanabria-Gonzalez, N. R.; *Sci. World J.* **2021**, *2021*, ID 9998924. [Crossref]

48. Akpotu, S. O.; Moodley, B.; *J. Mol. Liq.* **2018**, *261*, 540. [Crossref]

49. Hodali, H.A.; Rawajfeh, R. S.; Allababdeh, N.A.; *J. Dispersion Sci. Technol.* **2016**, *38*, 1342. [Crossref]

50. Yang, B.; Shi, J.; *Acc. Mater. Res.* **2021**, *2*, 581. [Crossref]

51. Patra, J. K.; Das, G.; Fraceto, L. F.; Campos, E. V. R.; Rodriguez-Torres, M. D. P.; Acosta-Torres, L. S.; Diaz-Torres, L. A.; Grillo, R.; Swamy, M. K.; Sharma, S.; Habtemariam, S.; Shin, H. S.; *J. Nanobiotechnol.* **2018**, *16*, 71. [Crossref]

52. Kesimli, B.; Topacli, A.; Topacli, C.; *J. Mol. Struct.* **2003**, *645*, 199. [Crossref]

53. Gunasekaran, S.; Sankari, G.; Ponnusamy, S.; *Spectrochim. Acta, Part A* **2005**, *61*, 117. [Crossref]

54. Aghaei, H.; Nourbakhsh, A. A.; Karbasi, S.; Javadkalbasi, R.; Rafienia, M.; Nourbakhsh, N.; Bonakdar, S.; MacKenzie, K. J. D.; *Ceram. Int.* **2014**, *40*, 7355. [Crossref]

55. Shah, P.; Rajput, S. J.; *Drug Dev. Ind. Pharm.* **2019**, *45*, 587. [Crossref]

56. Abukhadra, M. R.; Refay, N. M.; El-Sherbeeny, A. M.; El-Meligy, M. A.; *ACS Omega* **2020**, *5*, 11745. [Crossref]

57. Rosenholm, J. M.; Sahlgren, C.; Lindén, M.; *Nanoscale* **2010**, *2*, 1870. [Crossref]

58. Mendiratta, S.; Hussein, M.; Nasser, H. A.; Ali, A. A. A.; *Part. Part. Syst. Charact.* **2019**, *36*, 1900195. [Crossref]

59. Lee, W.-H.; Loo, C.-Y.; Traini, D.; Young, P. M.; *Expert Opin. Drug Delivery* **2015**, *12*, 1009. [Crossref]

60. Kamikubo, Y.; Yamana, T.; Hashimoto, Y.; Sakurai, T.; *ACS Chem. Neurosci.* **2019**, *10*, 304. [Crossref]